Room-temperature InP/InAsP Quantum Discs-in-Nanowire Infrared Photodetectors

Karimi, Mohammad; Jain, Vishal; Heurlin, Magnus; Nowzari, Ali; Hussain, Laiq; Lindgren, David; Stehr, Jan Eric; Buyanova, Irina A.; Gustafsson, Anders; Samuelson, Lars; Borgström, Magnus; Pettersson, Håkan

Published in:
Nano Letters

DOI:
10.1021/acs.nanolett.6b05114

2017

Document Version:
Peer reviewed version (aka post-print)

Room-temperature InP/InAsP Quantum Discs-in-nanowire Infrared Photodetectors

Mohammad Karimi,[1,2,‡] Vishal Jain,[1,2,‡] Magnus Heurlin,[1] Ali Nowzari,[1] Laiq Hussain,[1,2] David Lindgren,[1] Jan Eric Stehr,[3] Irina A. Buyanova,[3] Anders Gustafsson,[1] Lars Samuelson,[1] Magnus T. Borgström[1] and Håkan Pettersson[1,2]*

[1]Solid State Physics and NanoLund, Lund University, Box 118, SE-221 00 Lund, Sweden

[2]Department of Mathematics, Physics and Electrical Engineering, Halmstad University, Box 823, SE-301 18 Halmstad, Sweden

[3]Department of Physics, Chemistry and Biology, Linköping University, SE-581 83 Linköping, Sweden

ABSTRACT

The possibility to engineer nanowire heterostructures with large bandgap variations is particularly interesting for technologically important broadband photodetector applications. Here we report on a combined study of design, fabrication and optoelectronic properties of infrared photodetectors comprising 4 million n^+-i-n^+ InP nanowires periodically ordered in arrays. The nanowires were grown by metal-organic vapor phase epitaxy on InP substrates, with either a single or 20 InAsP quantum discs embedded in the i-segment. By Zn compensation of the residual n-dopants in the i-segment, the room-temperature dark current is strongly suppressed to a level of pA/NW at 1 V bias. The low dark current is manifested in the spectrally resolved photocurrent measurements, which reveal strong photocurrent contributions from the InAsP quantum discs at room temperature with a threshold wavelength of about 2.0 μm and a bias-tunable responsivity reaching 7 A/W@1.38 μm at 2 V bias. Two different processing schemes were implemented to study the effects of radial self-gating in the nanowires induced by the nanowire/SiO_x/ITO wrap-gate geometry. Summarized, our results show that properly designed axial InP/InAsP nanowire heterostructures are promising candidates for broadband photodetectors.

KEYWORDS: nanowires, infrared photodetectors, quantum discs, disc-in-nanowire

Semiconductor nanowires (NWs) have demonstrated their benefits for photonic and optoelectronic applications such as solar cells,[1, 2] lasers[3, 4] and photodetectors.[5, 6] The 1D geometry of NWs inherently provides strain relaxation for heterogeneous integration[7] and strong light mode confinement.[8] NW-based photonic devices have also been demonstrated to offer significantly enhanced quantum efficiency,[9] gain[10] and reduced noise.[11] Furthermore, the inclusion of low-dimensional quantum heterostructures in NWs adds new degrees of design freedom for optimization of electrical and optical performance. Room-temperature lasing in quantum dots embedded in single NWs,[12] ultrafast photodetectors based on core-shell NWs,[13] single exciton avalanche amplification[14] and disc-in-wire LEDs[15] are just a few examples which exploit low-dimensional quantum structures inside NWs. InP/InAsP heterostructures are of particular interest for high-speed electronic devices because of their excellent transport properties.[16] The relatively large conduction band offset in the InP/InAsP system strongly confines carriers leading to higher operating temperatures in lasers and lowers the leakage current in detectors.[17] Implementing this material system in a NW geometry combines the advantages of the small footprint, bandgap tuning and confinement in quantum discs (QDiscs) for ultimate monolithic integration of photonics with main-stream silicon CMOS driver/read-out electronics. Properly designed, such NW heterostructures represent an ideal material system to develop broadband photodetectors for applications in optical communication, surveillance and thermal imaging.

The so far few reported studies on NW-based photodetectors comprising optically active embedded quantum structures are strongly limited to single NW devices.[18, 19] One recently reported study on vertically processed random assemblies of InP NWs with embedded InAsP quantum dots, grown by MBE on Si (111),[20] exhibited a small dot-induced photocurrent (PC) signal and an overall reduced detector performance with only about 20% of the NWs properly aligned. In this Letter, we present infrared photodetectors based on large arrays of 4 million

InP NWs, grown by MOVPE in perfectly ordered vertical arrays, comprising single or multiple (20) InAsP QDiscs, on InP substrates. While typically a p^+-i-n^+ geometry is chosen for interband detectors, we focus here on an n^+-i-n^+ geometry, in combination with incorporated InAsP QDiscs, since we ultimately target broadband detectors offering both interband and intersubband photodetection capabilities. The high crystalline quality and tuned doping profile of the grown NW heterostructures, combined with an optimized device processing scheme, lead to a low dark current, a high responsivity and a spectral detection window extended to 2.0 μm at 300K.

We first present a detailed study of two different processing schemes, including complementary simulations, to find the optimum method for the fabrication of NW array detectors comprising a single QDisc in each NW. Subsequently, the number of QDiscs is increased to 20 to enhance their contribution to the interband photocurrent (PC) and possibly to reveal intersubband PC. In order to further improve the device performance, we compensated unintentional n-doping in the nominally intrinsic NW section by *in-situ* Zn doping. Results show that the use of Zn compensation leads to a drastically reduced dark current by about four orders of magnitude, yielding excellent room-temperature operation of the device. Finally, spectrally resolved PC data and cathodoluminescence (CL) imaging of the devices are presented and discussed.

For NW growth, n^+-InP (111)B substrates were patterned with Au particles by nanoimprint lithography, metal evaporation and lift-off.[21] The final pattern consisted of 20 nm thick Au discs with a 180 nm diameter, which during growth formed 130 nm diameter Au-In alloy particles. The center-to-center distance (pitch) between two Au particles was 400 nm. The growth was carried out in a low-pressure (100 mbar) Aixtron 200/4 MOVPE at 440 °C. The grown NWs had a diameter of 130 nm and a length of about 2 μm. In literature, non-intentionally doped InP NWs have been evaluated to be slightly n-type with electron

concentrations ranging from 10^{15} to 10^{16} cm^{-3} when grown by MBE[22] and MOVPE.[23] Such unintentional doping affects the performance of optoelectronic devices and might lead to, for instance, significantly higher dark current levels as discussed below. To study the effects of Zn compensation doping on device performance, a series of single QDisc-in-NW samples were grown with varying diethylzinc (DEZn) molar fractions added during growth of the nominally intrinsic segments. The InAsP QDiscs were grown by turning off the trimethylindium (TMIn) flow and replacing the phosphine (PH_3) with arsine (AsH_3) for 2 s.[24, 25] The detailed growth parameters are summarized in the Supporting Information Table S1.

The vertical processing of the NW arrays was conducted based on two different sample designs to unravel the role of electrostatic self-gating on the optoelectronic properties. The first scheme (Figure 1a) started with the deposition of 50 nm of SiO_x, followed by 5 nm of Al_2O_3, using atomic layer deposition (ALD). A photoresist (S1813) was spin-coated and back-etched in reactive ion etching (RIE) to expose 200-250 nm of the NW tips. The SiO_x and Al_2O_3 were removed from the exposed tips by BOE, and subsequently the gold catalyst particles were removed using H_2SO_4:H_2O (1:10) and KI/I_2 solutions[26]. Then the resist was stripped and 800×800 μm^2 device areas were defined by patterning a photoresist lifting layer on the samples by UV lithography. After exposure, the photoresist was hard baked at 200 °C for 30 min. A 50 nm NW side-wall coverage was obtained by sputtering indium tin oxide (ITO) as a transparent top contact. Prior to the sputtering step, any native oxides were removed using an H_2SO_4:H_2O (1:10) solution to avoid a potentially poor contact formation between the NWs and ITO. Finally, two layers of 20 nm Ti and 400 nm Au were evaporated as bondpads. In the second processing scheme (Figure 1b), the thick photoresist layer was hard-baked instead of being stripped after etching the Au nanoparticles and SiO_x from the NW tips. Then ITO was sputtered on top of the photoresist followed by evaporation of the Ti and Au contact layers.

Figure 1c shows the average resistivity of 25 devices, normalized to the number of NWs, for each of the four indicated DEZn molar fractions (i.e. in total 100 devices), processed according to the scheme in Figure 1a, obtained with +1 V applied bias to the substrate leaving the top ITO contact grounded. The average resistivity (around 10^3 Ωcm) for devices without Zn compensation was comparable to the previously reported (460 Ωcm) resistivity of n^+-i-n^+ InP NWs.[23] Adding DEZn in a molar fraction, χ_{DEZn}, of 0.5×10^{-7} during growth of the nominal i-segment increased the resistivity 100-fold to about 10^5 Ωcm. While the two samples with $\chi_{DEZn} = 1.4\times10^{-7}$ and $\chi_{DEZn} = 4.1\times10^{-7}$ showed even higher resistivity (Figure 1c), they also exhibited an open-circuit voltage under illumination (Supporting Information Figure S1). A probable reason is an overcompensation of the unintentional n^- doping in the i-segment by Zn, creating an n^+-p^--n^+ structure instead of an n^+-i-n^+ structure. The large error bar for the sample with $\chi_{DEZn}=1.4\times10^{-7}$ arises from the fact that more devices were included from the edges of the sample in this case. Devices near the edges typically exhibited a larger variation in leakage current due to processing-related issues. Based on these results, $\chi_{DEZn} = 0.5\times10^{-7}$ was selected as the optimum DEZn molar fraction.

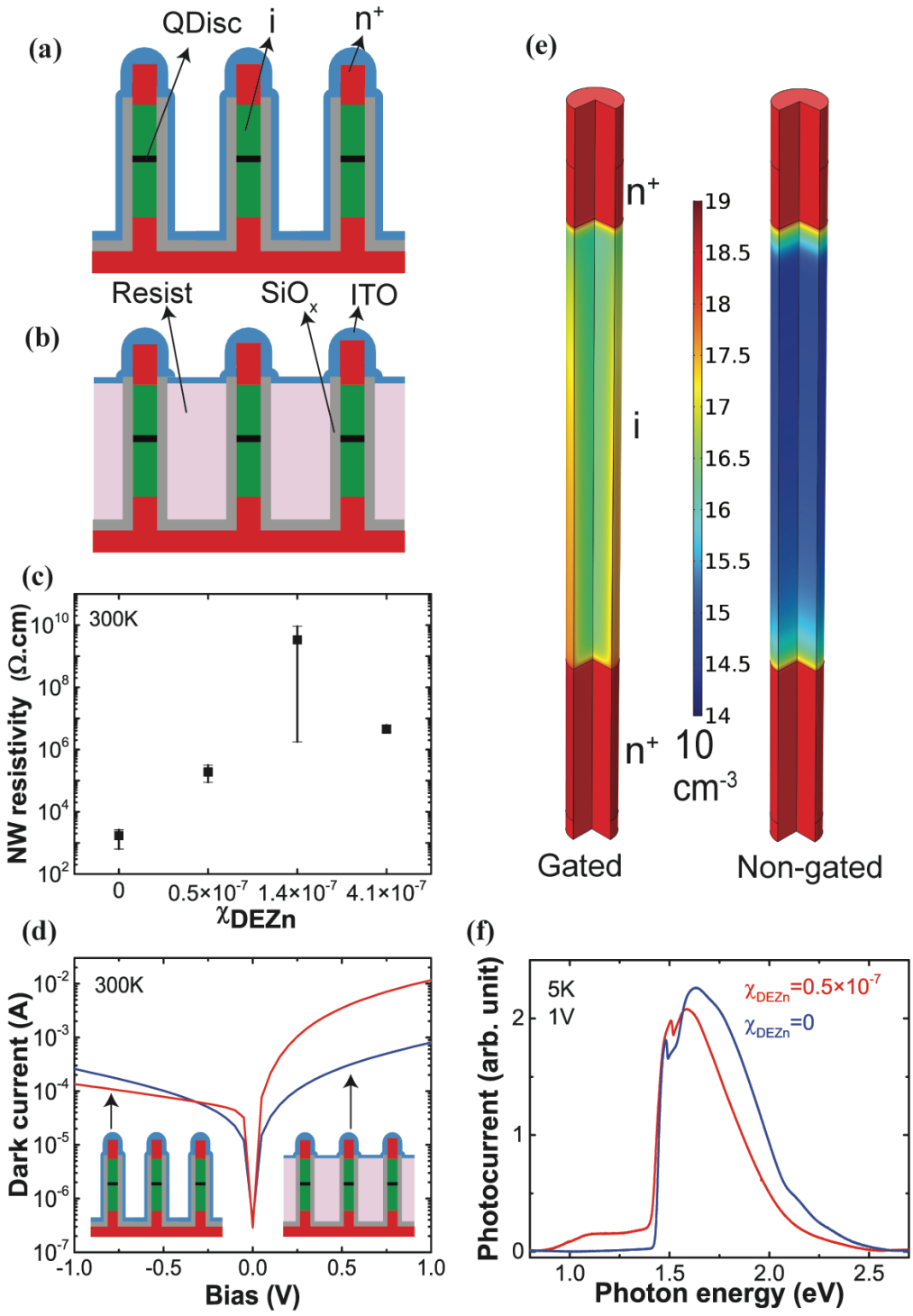

Figure 1. (a) First processing scheme with ITO on the sidewalls of the NWs. (b) Second processing scheme with ITO sputtered on top of the resist acting as spacer layer to prevent side-gating effects. (c) Average NW resistivity, with estimated error bars, of samples grown with different DEZn molar fractions and processed according to (a). (d) I-V characteristics of two array detectors grown with chosen Zn compensation. Red and blue traces correspond to devices processed according to (a) and (b),

respectively. (e) Simulated electron concentration in log scale for a NW processed according to gated and non-gated schemes in (a) and (b), respectively. (f) Spectrally resolved photocurrent for two detectors comprising a single QDisc in each NW, grown with chosen Zn compensation (red trace) and without Zn (blue trace), both processed according to (b).

We noted that the I-V characteristics for a typical device grown with the chosen DEZn molar fraction was quite asymmetric (red trace in Figure 1d). Asymmetric I-V characteristics have previously been reported in planar quantum well photodetectors and were attributed to different effects like dopant segregation[27] or growth-induced thickness modulation of the quantum well.[28] However, the asymmetry observed in our devices was on average significantly stronger than expected for any of the aforementioned effects (more than a factor of 20 in the ratio between dark currents recorded at 1 V and -1 V). Instead, we interpret this asymmetry in terms of self-gating induced by the ITO/SiO_x/NW wrap-gate geometry. Since the NW tip always has the same potential as the ITO covering the sidewalls, any applied bias could effectively induce carrier depletion/accumulation in the NWs which would change the spatial distribution of the carrier concentration and consequently the measured current. In order to verify this hypothesis, we fabricated another single QDisc-in-NW sample from the same growth run with $\chi_{DEZn} = 0.5\times10^{-7}$ (named sample A hereafter), but processed it according to the scheme in Figure 1b. The hard-baked photoresist in this case prevented the formation of an ITO/SiO_x/NW MOS-like structure and allowed only the tip of NWs to be in contact with ITO, eliminating any side-gating effects. Evidently, the I-V characteristics of sample A was significantly more symmetric (blue trace in Figure 1d) confirming a reduced accumulation (at positive bias) and depletion (at negative bias) of electrons in the NWs without self-gating. Figure 1e shows a theoretical comparison of induced self-gating (accumulation of electrons) in a NW processed according to the two investigated schemes using the semiconductor module of COMSOL (see Jain *et.al*[29] for more details). The conditions for the simulations were chosen

such that the tip was at +1 V bias with respect to the grounded base (i.e. the substrate in the case of an array device). Calculating the full I-V characteristics using the same model indeed showed asymmetric characteristics for NWs processed according to the side-gated processing scheme (Supporting Information Figure S2).

Spectrally resolved photocurrent (PC) measurements were carried out on array detectors both with Zn compensation (sample A) and without Zn. Evidently, the interband photocurrent from the InAsP QDiscs starting at 0.9 eV was much more prominent with added Zn (Figure 1f) due to the dark current reduction and an enhanced collection of photogenerated carriers induced by a better optimized electric field distribution.

After optimization of the χ_{DEZn} molar fraction and growth parameters for a single QDisc device (Supporting Information Table S1), we incorporated 20 QDiscs into the i-segment in each NW in order to increase the photocurrent. Optimized growth parameters (Supporting Information Table S2) were found after several growth test runs. The grown NWs had a diameter of 130 nm and a length of 2 μm (Figure 2a), similar to the sample A. The grown QDiscs had thicknesses of 10±1 nm, as observed in TEM (Figure 2b). Energy dispersive X-ray spectroscopy (EDX) revealed sharp InAsP/InP interface transitions (Figure 2b). Point measurements of the composition in the QDiscs yielded As concentrations between 60-80 %. The separation between the QDiscs varied from 50 nm at the base to 25 nm at the tip of the NWs (Figure 2d). This decrease in InP barrier thickness is consistent with the drop in growth rate with length of pure InP NWs which occurs due to a decreased In supply from the substrate surface.[30] Photoluminescence (PL) measurements revealed a relatively broad peak between 0.9 eV and 1.2 eV at 5 K (Figure 2c). The peak width most likely reflects the combination of variations in QDisc thickness and composition.[15, 20] A simple estimate of the wurtzite $InAs_xP_{1-x}$ bandgap would be 0.67-0.86 eV for $0.6 < x < 0.8$ (estimated from EDX) using an InAs and InP WZ bandgap of 0.48 eV,[31] and 1.49 eV,[32] respectively, and a bowing parameter of 0.1 eV[33]

at 4 K. The observed blue-shift in PL compared to the estimated bandgap of the QDiscs can be explained by quantum confinement as estimated from both a simple unstrained disc model, as well as from sophisticated k·p calculations assuming a planar (strained) quantum well model. We note that similar results have been reported elsewhere[20, 24]. A detailed calculation of the electronic structure for the present strain-relaxed QDiscs is beyond the scope of this work. It should be mentioned here that no passivating shell was grown on these NWs. Due to the highly doped n^+-segments of the n^+-i- n^+ NWs, there is a risk that even a non-intentionally doped shell might lead to a significant parasitic shunt leakage current. Moreover, the NWs evidently exhibited a strong PL signal even though they were unpassivated, in contrast to previously reported MBE grown NWs[20]. This points to a reduced number of surface states and lower surface recombination velocity in the present NWs.[34] To make the comparison fair, it should be mentioned that the NWs in Ref. 20 had significantly smaller diameter (60 nm) than the NWs studied in this work, resulting in a much higher surface-to-volume ratio, which has a significant influence on the emission intensity.

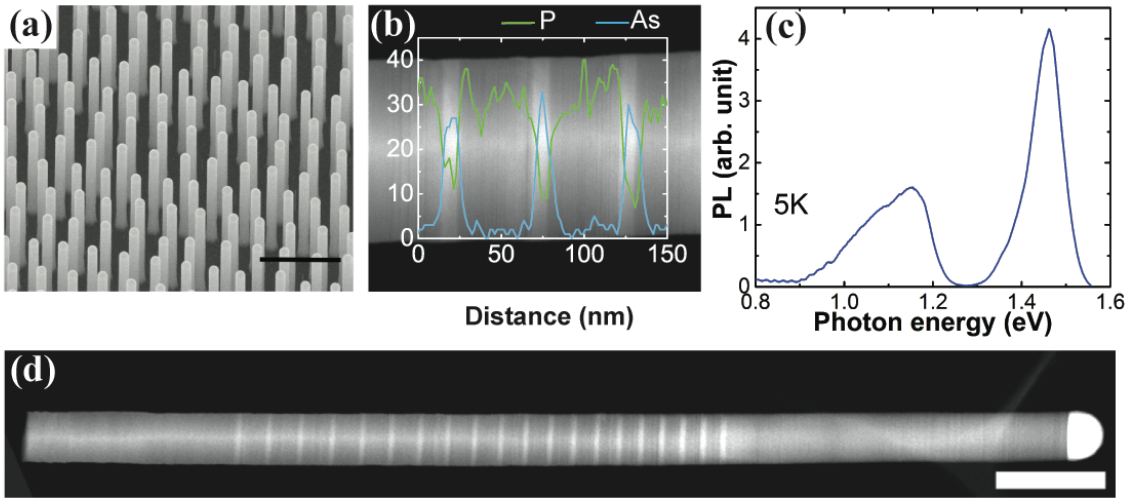

Figure 2. (a) SEM image of an as-grown InP n^+-i-n^+ NW array with 20 InAsP QDiscs in each NW. The scale bar is 1 µm. (b) EDX linescans overlaid on a TEM image of a NW. Green (blue) color represents

P (As), respectively. (c) Typical PL and (d) TEM of a representative NW. The scale bar is 200 nm.

Based on the results discussed above, the 20 QDiscs-in-NW samples were grown without (sample B) and with added Zn of $\chi_{DEZn} = 0.5\times10^{-7}$ (sample C). Table 1 below summarizes an overview of the different investigated samples. The samples were processed with a thick photoresist spacer layer, similar to sample A (Figure 1b and more detailed Figure 3a below). A strong temperature dependence of the dark current was observed for sample B, with a reduction of about four orders of magnitude at 2 V bias from 300 K to 5 K (Figure 3b). Such strong temperature dependence was not observed in sample A (Supporting Information Figure S3), indicating efficient trapping of carriers at low temperatures in the staggered potential landscape introduced by the multiple QDiscs. Fig. S4 shows an Arrhenius plot of the dark current for sample B at different applied biases. The activation energy of 0.12 eV at 0.10 V bias reflects the energy separation between the Fermi-level in the discs and the InP conduction band edge. A decrease in activation energy upon increasing the applied bias is attributed to various barrier lowering escape mechanisms, including the Poole-Frenkel effect and phonon-assisted tunneling. Sample C (with added Zn) exhibited more than four orders of magnitude reduced dark current over a broad temperature range compared to sample B (Figure 3c), pointing to an efficient compensation of residual n-dopants by Zn in the i-segment. The inset of Fig. S4 shows the corresponding Arrhenius plot of the dark current at a bias of 0.70 V. The obtained activation energy of 0.43 eV is significantly higher compared to that of sample B, confirming the efficient compensation of residual n-dopants by Zn and a lowering of the Fermi-level to the bottom of the discs. Here we note that the conduction band offset between nearly unstrained InAs and InP segments in 40 nm thick NWs amounts to about 0.6 eV.[35] The strong reduction in dark current in sample C led to a very high photocurrent-to-dark current ratio, I_{ph}/I_{dark}, of up to 10^5 at 5 K (inset of Figure 3c) calculated from the ratio between the

photocurrent and dark current at -2 V bias shown in Fig. S5.

Sample	Description	χ_{DEZn}
A	Single QDisc-in-NW	0.5×10^{-7}
B	20 QDiscs-in-NW	0
C	20 QDiscs-in-NW	0.5×10^{-7}

Table 1. Overview of samples A, B and C

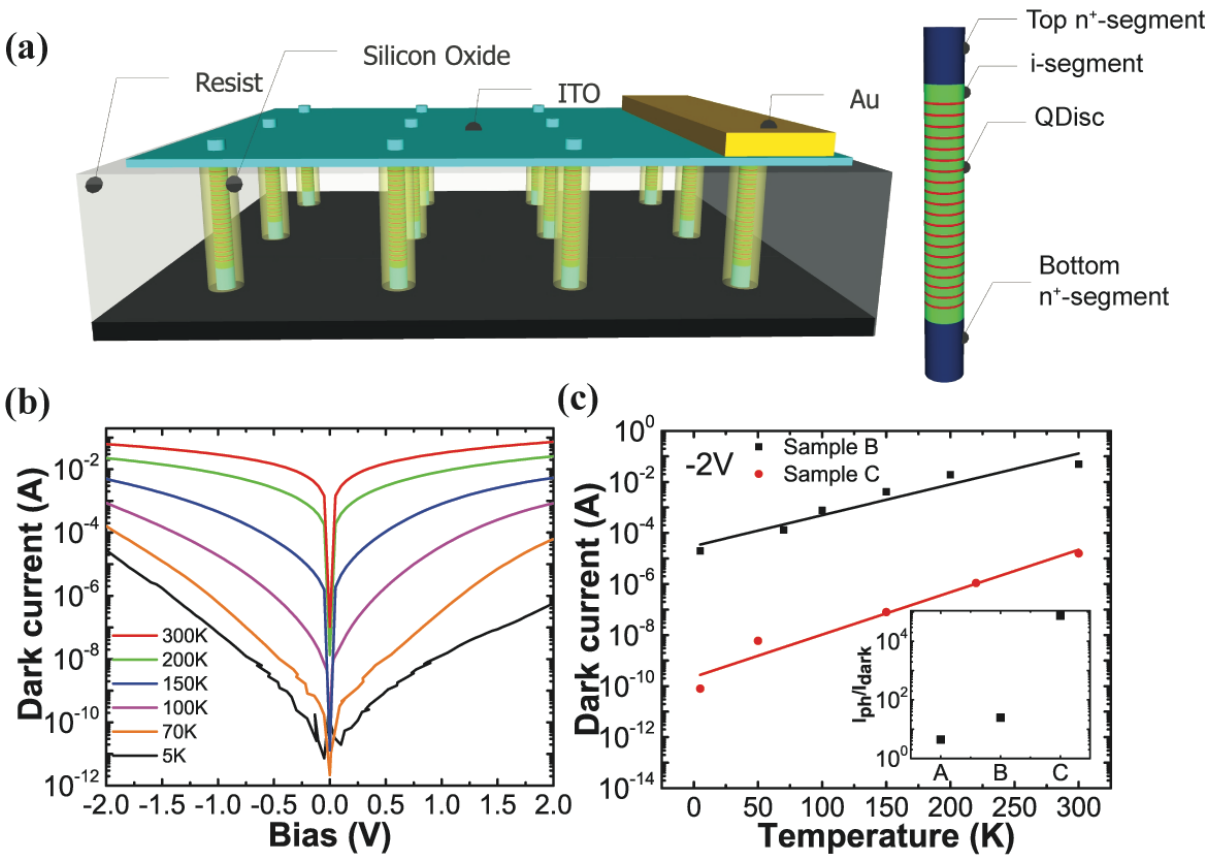

Figure 3. (a) Schematics of a vertically processed 20 QDiscs-in-wire array detector. (b) Temperature dependence of the dark I-V characteristics of sample B (without Zn). (c) Comparison of the dark current at -2 V bias of sample B and C at different temperatures. The inset highlights the trend of increasing I_{ph}/I_{dark} by introducing multiple discs and adding Zn (T=5 K).

Figure 4a shows the spectrally resolved photocurrent of samples B and C measured at 5K. Clear spectral signatures of InP ZB and WZ crystal structures were visible in both samples as

reported previously.[36] The PC with onset of about 0.75 eV is attributed to the QDiscs. The QDisc interband PC exhibits a broad signal with several peaks, which can be explained by thickness and compositional variations of the QDiscs, or by different electronic transitions in the QDiscs. Figure 4b shows the corresponding room-temperature PC of sample C at varying applied bias. A general observation is that the PC is strongly enhanced with increasing temperature. The integrated (all-wavelength) PC extracted from I-V measurements under illumination at a bias of -0.7 V enhances by a factor of 500 from 100 nA to 50 μA comparing 300 K and 5 K (not shown here). The onset of about 0.60 eV at 300 K is red-shifted compared to the 5 K onset by about 150 meV, which can be attributed to both the temperature-dependence of the bandgap (about 70 meV)[31, 37] and to an enhanced thermal excitation of photogenerated carriers from the QDiscs to the InP NW matrix. The QDisc PC enhances significantly with increasing photon energy and bias since final states in the optical transitions are closer to the InP conduction band edge, facilitating enhanced escape mechanisms through photo-thermal emission, phonon-assisted tunneling and the Poole-Frenkel effect. The relative PC contribution from the QDiscs compared to the InP NW matrix is also enhanced at 300 K compared to 5 K, indicating that the photogenerated carriers are more efficiently extracted from the QDiscs by thermal activation.

Similar behavior showing increased PC with increasing temperature has previously been reported in single NWs with multiple Q-discs.[18] It is also obvious from Figure 4b that an increasing applied bias facilitates an improved symmetric carrier extraction, as expected from an n^+-i-n^+ photoconductor without significant built-in electric field. It should be noted that the photocurrent from sample B (Figure S6 in Supporting Information) was very weak compared to sample C at 300 K confirming the success of using Zn for compensation doping in order to suppress the dark current. Figure 4c shows the spectrally resolved responsivity of sample C, extracted from the PC data in Fig. 4b using calibrated photodiodes. In order to cover the full

spectral range of the NW detector, both Ge and Si photodiodes had to be used to extract the responsivity. Evidently, the relative contribution from the QDiscs, compared to the InP NW matrix, appears reduced compared to the PC presented in Fig 4b. This is due to a reduced transmission of the CaF_2 beam-splitter, and a weakly reduced intensity from the quartz lamp, in the range 1.1-2.4 eV. It should be noted, however, that the responsivity in the spectral region covered by the QDiscs amounts to 0.6 A/W (at 0.9 eV), steadily increasing with applied bias to 7 A/W at 2 V bias (inset of Fig. 4c). This value is significantly higher than the typical responsivity of commercially available InGaAs, Ge and Si photodiodes (the calibrated detectors used in this study both have a peak responsivity < 1A/W).

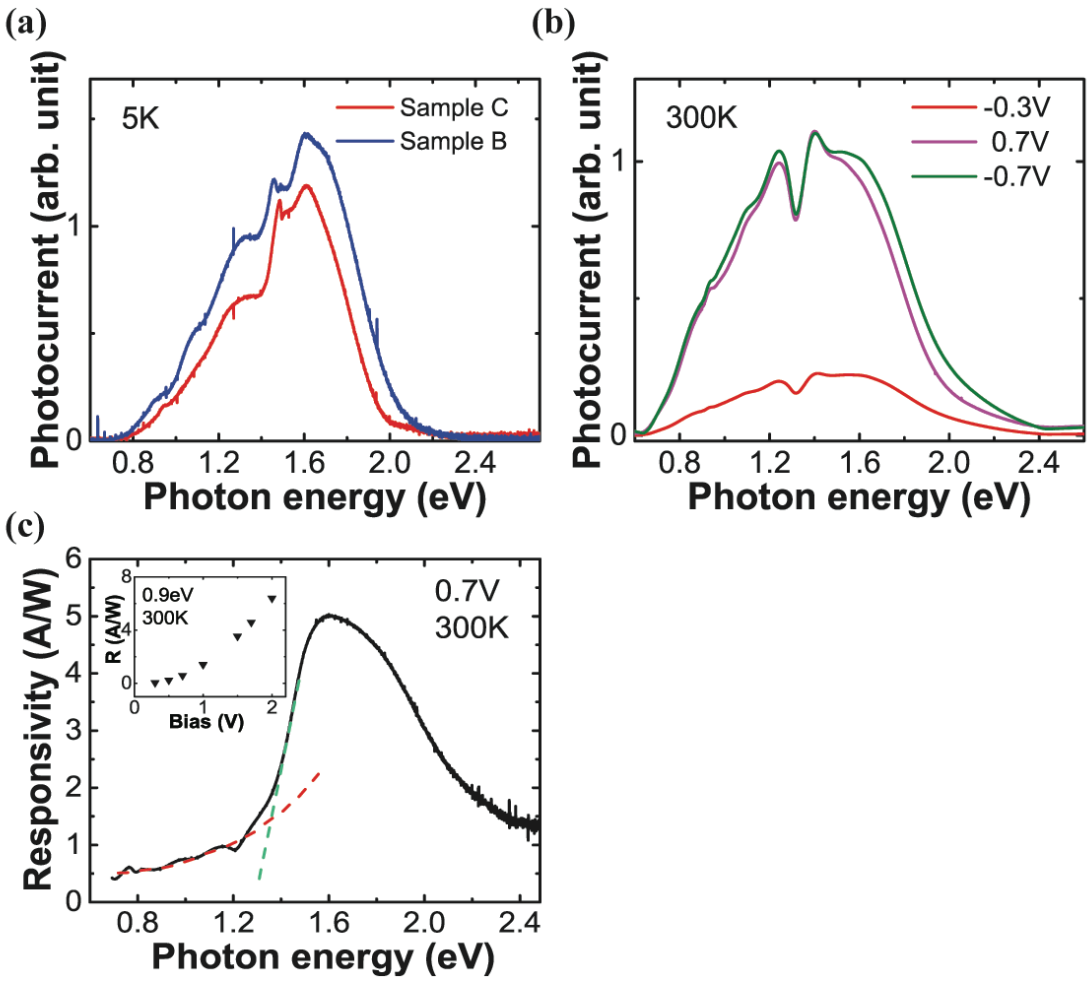

Figure 4. Spectrally resolved PC for (a) samples B and C at 5 K and -0.3 V applied bias and (b) sample C at 300 K for varying applied biases. (c) Spectrally resolved responsivity of sample C at 300 K and

0.7 V bias. The dashed colored lines are guidelines for the eye, indicating contributions from the QDiscs and InP NW, respectively. The inset shows the responsivity as a function of applied bias at 0.90 eV (1.38 μm).

Cathodoluminescence (CL) spectroscopy was finally carried out to do spatial mapping of the luminescence from single NWs containing either a single or 20 QDiscs in the Zn-doped i-segment. The mapping was done using a Si CCD detector, which is blind for the QDisc emission, but sensitive to the InP emission. Figure 5 shows the data from a single NW comprising 20 embedded QDiscs (sample C). Most of the NWs show bandgap emission related to InP, with a blue shift towards the top of the NW. This is consistent with the trend observed in TEM of an increasing WZ content towards the tip of the NW. A more interesting feature is that the InP emission is absent from the entire i-segment, confirmed by a comparison with a HAADF TEM image of another NW from the same growth run. This confirms the previous indication of QDiscs acting as efficient traps for carriers, consistent with the very low dark current observed for corresponding processed array devices containing these NWs. An analysis of the intensity profile[38] for a corresponding NW with a single embedded QDisc (Figure S7 in Supporting Information) shows similar behavior with a void in the InP emission at the position of the disc. Further analysis of the CL from this sample revealed a diffusion length of about 100–200 nm, similar to values recorded for InP p-n junctions.[39]

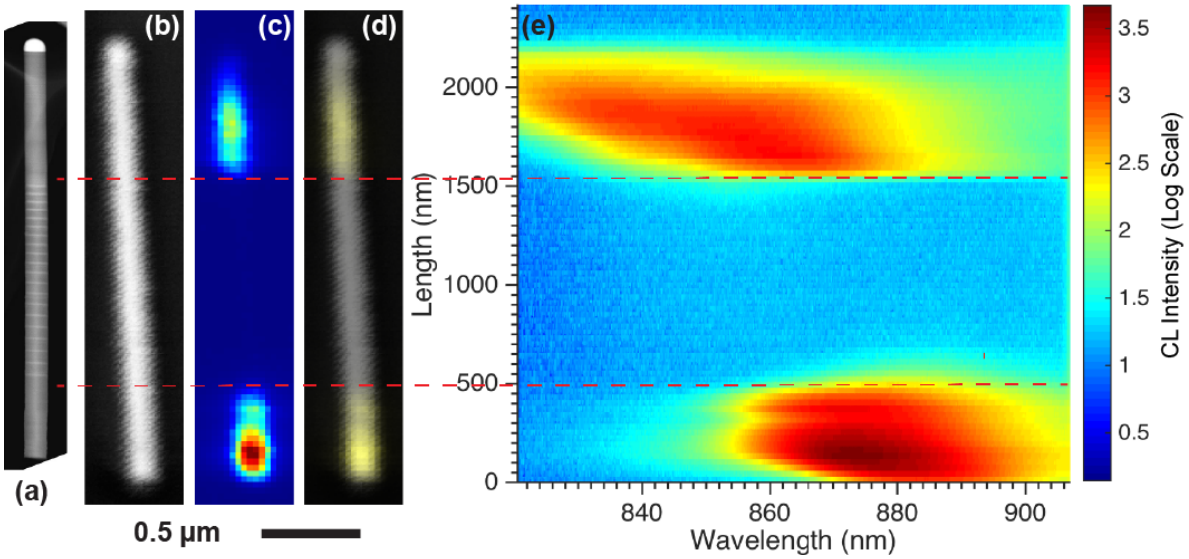

Figure 5. Hyperspectral imaging of a NW with 20 QDiscs transferred to a Si substrate. (a) HAADF TEM image of a similar NW. (b) SEM image recorded at the same time as the hyperspectral data. (c) Panchromatic CL image (linear scale – 830 to 910 nm). (d) Composite image of (b) and (c). (e) Hyperspectral map of the emission along the wire in log scale.

In conclusion, we report on design, fabrication and characterization of n^+-i-n^+ InP NW array photoconductors, comprising single or 20 inserted InAsP QDiscs in each NW, grown by MOVPE. Adding Zn to the i-segment of the NWs reduces the dark current by four orders of magnitude to pA/NW at 1 V bias at 300 K in the multiple QDisc samples. From spectrally resolved photocurrent measurements it was concluded that the QDiscs provide a strong photocurrent contribution with a bias-tunable responsivity reaching 7 A/W@1.38 µm at 2 V bias, and a significantly extended spectral sensitivity window to about 0.60 eV (2.0 µm) at room-temperature. The effect of radial depletion, induced by an effective wrap-gate design, on the I-V characteristics was examined both experimentally as well as by simulations. The results show promising potential for large array NW photodetectors comprising incorporated quantum

heterostructures for broadband detection applications.

Experimental Setup.

Initial I-V test measurements were performed at 300 K using a Cascade 11000B probe station in conjunction with a Keithley 4200 semiconductor characterization system. After mounting the samples on DIL-14 holders and bonding, PC measurements were done using a Bruker Vertex 80v Fourier transform infrared (FTIR) spectrometer housing an integrated variable temperature Janis PTSHI-950-FTIR pulse-tube closed-cycle cryostat. The spectrometer was equipped with a CaF_2 beamsplitter and a quartz lamp and was evacuated to avoid any influence of absorption lines in air. The intensity of the quartz lamp is about 10-15mW/cm^2 in the spectral range from 500 nm-1100 nm. The modulated (~7.5 kHz) PC was amplified using a Keithley 428 programmable current amplifier. Any (non-modulated) DC contributions, e.g. dark current, are automatically removed in FTIR PC spectroscopy. Variable temperature (5 K – 300 K) I-V measurements were recorded with a Keithley 2636 sourcemeter.

Spatially and spectrally resolved cathodoluminescence (CL) investigations were performed at low temperature (8K) on individual NWs using a dedicated scanning electron microscope (SEM). A Si CCD detector was used for hyperspectral imaging. The studies were performed at 5 kV and a probe current of 10 – 500 pA.

ASSOCIATED CONTENT

Supporting Information

The Supporting Information is available free of charge on the ACS Publications website at DOI: 10.1021/acs.nanolett. 6b05114. Growth parameters, I−V characteristics, simulated I−V curves comparing effects of side-gating, temperature dependence of the dark current versus bias, Arrhenius plots of the dark current, typical I−V characteristics in darkness and under

illumination, spectrally resolved photocurrent, and hyperspectral cathodoluminescence imaging (PDF)

AUTHOR INFORMATION

Corresponding Author

* hakan.pettersson@hh.se

‡ Mohammad Karimi and Vishal Jain contributed equally to this work.

All authors have given approval to the final version of the manuscript.

ACKNOWLEDGEMENTS

We thank Gaute Otnes for fruitful discussions on nanowire growth and Reza Jafari Jam for help with processing. The authors acknowledge financial support from NanoLund, the Swedish Research Council, the Swedish National Board for Industrial and Technological Development, the Swedish Foundation for Strategic Research and the Swedish Energy Agency, the Erik Johan Ljungberg Foundation and the Carl Trygger Foundation. This project has received funding from the European Union's Horizon 2020 research and innovation program under grant agreement No 641023 (NanoTandem).

REFERENCES

1. Wallentin, J.; Anttu, N.; Asoli, D.; Huffman, M.; Åberg, I.; Magnusson, M. H.; Siefer, G.; Fuss-Kailuweit, P.; Dimroth, F.; Witzigmann, B. *Science* **2013,** 339, (6123), 1057-1060.
2. Åberg, I.; Vescovi, G.; Asoli, D.; Naseem, U.; Gilboy, J. P.; Sundvall, C.; Dahlgren, A.; Svensson, K. E.; Anttu, N.; Björk, M. T. *IEEE J. Photovolt.* **2016,** 6, (1), 185-190.

3. Liu, Z.; Yin, L.; Ning, H.; Yang, Z.; Tong, L.; Ning, C.-Z. *Nano letters* **2013,** 13, (10), 4945-4950.
4. Zhu, H.; Fu, Y.; Meng, F.; Wu, X.; Gong, Z.; Ding, Q.; Gustafsson, M. V.; Trinh, M. T.; Jin, S.; Zhu, X. *Nat. Mater.* **2015,** 14, (6), 636-642.
5. Thompson, M. D.; Alhodaib, A.; Craig, A. P.; Robson, A.; Aziz, A.; Krier, A.; Svensson, J.; Wernersson, L.-E.; Sanchez, A. M.; Marshall, A. R. *Nano Lett.* **2015,** 16, (1), 182-187.
6. Pettersson, H.; Trägårdh, J.; Persson, A. I.; Landin, L.; Hessman, D.; Samuelson, L. *Nano Lett.* **2006,** 6, (2), 229-232.
7. Svensson, C. P. T.; Mårtensson, T.; Trägårdh, J.; Larsson, C.; Rask, M.; Hessman, D.; Samuelson, L.; Ohlsson, J. *Nanotechnology* **2008,** 19, 305201.
8. Cao, L.; White, J. S.; Park, J.-S.; Schuller, J. A.; Clemens, B. M.; Brongersma, M. L. *Nat. Materials* **2009,** 8, 643-647.
9. Yang, Y.; Peng, X.; Hyatt, S.; Yu, D. *Nano Lett.* **2015,** 15, (5), 3541-3546.
10. Yan, R.; Gargas, D.; Yang, P. *Nat Photon* **2009,** 3, (10), 569-576.
11. Dai, X.; Zhang, S.; Wang, Z.; Adamo, G.; Liu, H.; Huang, Y.; Couteau, C.; Soci, C. *Nano letters* **2014,** 14, (5), 2688-2693.
12. Tatebayashi, J.; Kako, S.; Ho, J.; Ota, Y.; Iwamoto, S.; Arakawa, Y. *Nature Photonics* **2015,** 9, (8), 501-505.
13. Erhard, N.; Zenger, S.; Morkötter, S.; Rudolph, D.; Weiss, M.; Krenner, H. J.; Karl, H.; Abstreiter, G.; Finley, J. J.; Koblmüller, G. *Nano letters* **2015,** 15, (10), 6869-6874.
14. Bulgarini, G.; Reimer, M. E.; Hocevar, M.; Bakkers, E. P. A. M.; Kouwenhoven, L. P.; Zwiller, V. *Nat. Phot.* **2012,** 6, 455-458.
15. Yan, L.; Jahangir, S.; Wight, S. A.; Nikoobakht, B.; Bhattacharya, P.; Millunchick, J. M. *Nano letters* **2015,** 15, (3), 1535-1539.
16. Beaudoin, M.; Bensaada, A.; Leonelli, R.; Desjardins, P.; Masut, R.; Isnard, L.; Chennouf, A.; L'Espérance, G. *Physical Review B* **1996,** 53, (4), 1990.
17. Dixit, V.; Singh, S.; Porwal, S.; Kumar, R.; Ganguli, T.; Srivastava, A.; Oak, S. *Journal of Applied Physics* **2011,** 109, (8), 083702.
18. Rigutti, L.; Tchernycheva, M.; De Luna Bugallo, A.; Jacopin, G.; Julien, F.; Zagonel, L. F.; March, K.; Stephan, O.; Kociak, M.; Songmuang, R. *Nano letters* **2010,** 10, (8), 2939-2943.
19. Lahnemann, J.; Den Hertog, M.; Hille, P.; de la Mata, M. a.; Fournier, T.; Schörmann, J. r.; Arbiol, J.; Eickhoff, M.; Monroy, E. *Nano Lett.* **2016,** 16, (5), 3260-3267.
20. Kuyanov, P.; LaPierre, R. *Nanotechnology* **2015,** 26, (31), 315202.
21. Otnes, G.; Heurlin, M.; Graczyk, M.; Wallentin, J.; Jacobsson, D.; Berg, A.; Maximov, I.; Borgström, M. T. *Nano Research*, 1-10.
22. Yamada, T.; Yamada, H.; Lohn, A. J.; Kobayashi, N. P. *Nanotechnology* **2010,** 22, (5), 055201.
23. Wallentin, J.; Ek, M.; Wallenberg, L. R.; Samuelson, L.; Borgström, M. T. *Nano Lett.* **2012,** 12, (1), 151-155.
24. Sköld, N.; Pistol, M.-E.; Dick, K. A.; Pryor, C.; Wagner, J. B.; Karlsson, L. S.; Samuelson, L. *Phys. Rev. B* **2009,** 80, (041312).
25. Fröberg, L. E.; Wacaser, B. A.; Wagner, J. B.; Jeppesen, S. r.; Ohlsson, B. J.; Deppert, K.; Samuelson, L. *Nano Lett.* **2008,** 8, (11), 3815-3818.
26. Berg, A.; Yazdi, S.; Nowzari, A.; Storm, K.; Jain, V.; Vainorius, N.; Samuelson, L.; Wagner, J. B.; Borgstrom, M. T. *Nano Lett.* **2015,** 16, (1), 656-662.
27. Ravikumar, A. P.; Chen, G.; Zhao, K.; Tian, Y.; Prucnal, P.; Tamargo, M. C.; Gmachl, C. F.; Shen, A. *Applied Physics Letters* **2013,** 102, (16), 161107.
28. Chin, A.; Liao, C.; Chu, J.; Li, S. *Journal of crystal growth* **1997,** 175, 999-1003.

29. Jain, V.; Heurlin, M.; Karimi, M.; Hussain, L.; Aghaeipour, M.; Nowzari, A.; Berg, A.; Nylund, G.; Capasso, F.; Samuelson, L.; Borgström, M. T.; Pettersson, H. *Nanotechnology* **2017,** *Nanotechnology* 28, 11 (2017).
30. Heurlin, M.; Anttu, N.; Camus, C.; Samuelson, L.; Borgström, M. T. *Nano letters* **2015,** 15, (5), 3597-3602.
31. Rota, M. B.; Ameruddin, A. S.; Fonseka, H. A.; Gao, Q.; Mura, F.; Polimeni, A.; Miriametro, A.; Tan, H. H.; Jagadish, C.; Capizzi, M. *Nano Lett.* **2016,** 16, (8), 5197-5203.
32. Mishra, A.; Titova, L. V.; Hoang, T. B.; Jackson, H. E.; Smith, L. M.; Yarrison-Rice, J. M.; Kim, Y.; Joyce, H. J.; Gao, Q.; Tan, H. H.; Jagadish, C. *Appl. Phys. Lett.* **2007,** 91, 263104.
33. Vurgaftman, I.; Meyer, J. R.; Ram-Mohan, L. R. *J. Appl. Phys.* **2001,** 89, (11), 5815-5875.
34. Joyce, H. J.; Wong-Leung, J.; Yong, C.-K.; Docherty, C. J.; Paima, S.; Tan, Q. G. H.; Jagadish, C.; Lloyd-Hughes, J.; Herz, L. M.; Johnston, M. B. *Nano Lett.* **2012,** 12, 5325-5330.
35. Björk, M.; Ohlsson, B.; Sass, T.; Persson, A.; Thelander, C.; Magnusson, M.; Deppert, K.; Wallenberg, L.; Samuelson, L. *Nano Letters* **2002,** 2, (2), 87-89.
36. Jain, V.; Nowzari, A.; Wallentin, J.; Borgström, M.; Messing, M.; Asoli, D.; Graczyk, M.; Witzigmann, B.; Capasso, F.; Samuelson, L.; Pettersson, H. *Nano Res.* **2014,** 7, (4), 544-552.
37. Mattila, M.; Hakkarainen, T.; Mulot, M.; Lipsanen, H. *Nanotechnology* **2006,** 17, (6), 1580.
38. Gustafsson, A.; Bolinsson, J.; Sköld, N.; Samuelson, L. *Appl. Phys. Lett.* **2010,** 97, (7), 072114.
39. Wallentin, J.; Wickert, P.; Ek, M.; Gustafsson, A.; Wallenberg, L. R.; Magnusson, M. H.; Samuelson, L.; Deppert, K.; Borgström, M. T. *Appl. Phys. Lett.* **2011,** 99, (25), 253105.